Structure-correlated excitation wavelength-dependent optical properties of ZnO nanostructures for multifunctional applications

Dhritiman Banerjee[1], Payal Banerjee[2], Asit Kumar Kar[1]*

[1]Micro and Nano Science Laboratory, Department of Physics, Indian Institute of Technology (Indian School of Mines), Dhanbad, Jharkhand, 826004, India

[2] Department of Chemistry, National Tsing Hua University, Hsinchu, 300044, Taiwan (R.O.C.)

***Corresponding author:** banerjeegora90@gmail.com*

S1. Morphology and growth mechanisms of ZnO nanostructures

S1.1. Growth mechanism of electrodeposited ZnO nanorods over ITO

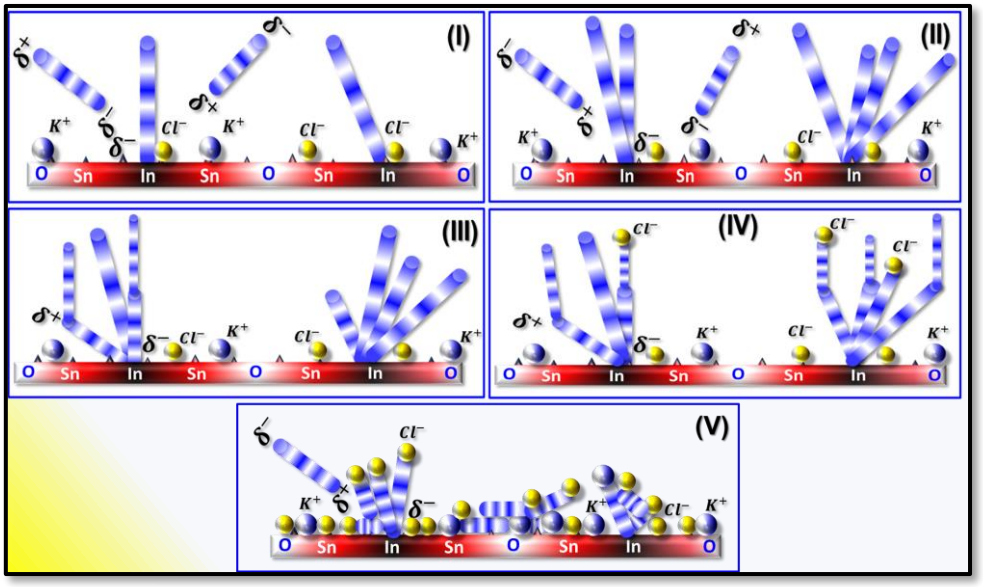

Fig. S1. Schematic illustration of the growth of the ZnO nanorods: **(I)** Selection of attachment of ZnO nanoparticles over ITO glass based upon electronegativity difference between the atoms of ITO. **(II)** Multiple attachments of inclined nanorods over ITO based on surface roughness. **(III)** Growth of secondary nanorods over others through attachment to the polar face of the grown nanorod. **(IV)** Adsorption of ions based termination of growth of nanorods. **(V)** Suppression of growth of nanorods at higher concentrations of KCl.

S1.2. Morphology of nanostructures obtained with ethanol as solvent by direct precipitation

As written below, the following reactions give rise to flake-like nanostructures in the ethanol medium.

$$Zn(OAc)_2.2H_2O \xrightarrow{Ethanol} Zn(OH)_2 + CH_3COOH \quad (1)$$

$$Zn(OH)_2 \longrightarrow [Zn(OH)_4]^{2-} + K^+ \quad (2)$$

$$Zn(OH)_2 \longrightarrow [Zn(OH)_4]^{2-} + H^+ \quad (3)$$

$$[Zn(OH)_4]^{2-} + 2H^+ \longrightarrow ZnO + H_2O + 2OH^- \quad (4)$$

$$Zn(OH)_2 \rightleftharpoons Zn^{2+} + 0H^- \quad (5)$$

$$Zn^{2+} + 2OH^- + C_2H_5OH \longrightarrow Zn(OH)_4^{2-} + 0H^- \quad (6)$$

- **Growth mechanism of nanoflakes and its shape evolution prepared in ethanol as solvent**

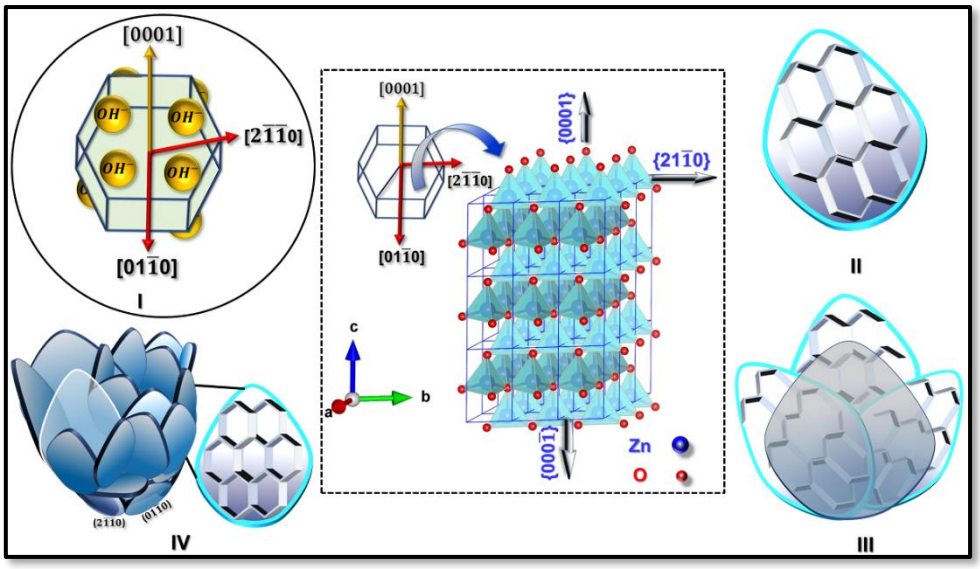

Fig. S2. Schematic diagram showing the four step-growth mechanisms of nanoflakes sample: **(I)** Hydroxide ions adsorbed over the (0001) surface of ZnO nanocrystals suppresses the growth along [0001] direction that leads to plate-like morphology. **(II)** Ordered arrangement of nanoplates leads to nanoflake morphology. **(III)** Arrangement of nanoflakes in a systematic way. **(IV)** Arrangement of nanoflakes in a way to generate close-packed morphology.

- **Evolution of the morphology from nanoflake to agglomerated nanosphere on variation in KOH concentration to 0.6 M inside the reaction medium in ethanol**

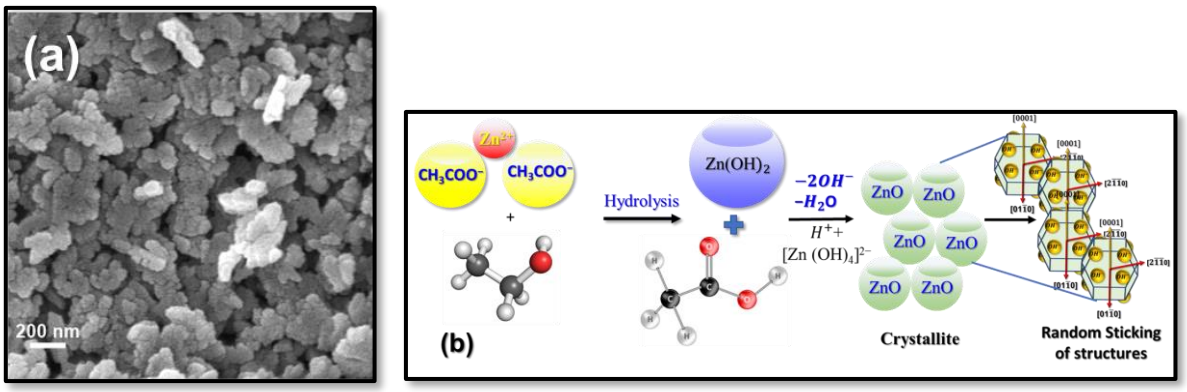

Fig S3. SEM Micrograph (2 µm × 2 µm) image of agglomerated ZnO nanoparticles grown in ethanol medium with 0.1 M zinc acetate [$Zn(CH_3COO)_2{\cdot}2H_2O$] and 0.6 M potassium hydroxide (KOH). (b) Schematic illustration of the formation of ZnO nanospheres and its subsequent aggregation during the growth of ZnO nanoparticles.

Mechanism: With the increase in the concentration of potassium hydroxide from 0.5 M to 0.6 M, the morphology of ZnO changes from nanoflakes to agglomerated nanosphere, as shown in Fig. S3(a). This is because the generated nuclei grow in size due to the high concentration of nuclei generated at the early stage of the reaction. This growth is due to a phenomenon known as coalescence, which leads to the sticking of generated nanosphere of ZnO hexagonal nuclei randomly, as shown in part in Fig. S3(b). Repetition of the ZnO hexagonal nuclei in an organised fashion gives rise to the ZnO nanosphere structure. The nanospheres are favoured instead of nanoplates as the system tries to minimise the surface energy of the ZnO nuclei by forming the nanosphere, which has the highest surface area to volume ratio with a non-preferential growth direction. These nanosphere agglomerates give rise to uneven random morphology.

S1.3. Structural properties of nanostructures: Crystallite size, W-H plots and Rietveld analysis

We have calculated the nanocrystallite size (*D*) for different nanostructures and measured the amount of strain present from the XRD spectra using the Debye-Scherrer formula given by Eqn. (7) and Williamson-Hall equations given in Eqn. (8), respectively.

Debye−Scherrer's formula is given below:

$$D = \frac{0.89\lambda}{\beta cos\theta} \qquad (7)$$

In this equation (11), the wavelength λ of Cu k_α radiation is 1.54 Å, β is the full width at half maximum (FWHM) of the peak, and θ is the Bragg's angle obtained from the 2θ values.

The crystallite size values for nanorods, nanothorns and nanoflakes are 14.9 nm, 16.7 nm, and 17.3 nm, respectively.

Hall-Williamson plots: The strain in the nanostructure has been determined from the Williamson-Hall plots given in Fig. S4 using the W-H equation given by Eqn. (8).

The Williamson-Hall equation is written as follows:

$$\beta cos\theta = \frac{0.89\lambda}{D} + 4\,\varepsilon\, Sin\theta \qquad (8)$$

Where, β represents the full width at half maximum (FWHM), D represents the crystallite size, ε as strain, θ is the diffraction angle, and λ is the wavelength (λ = 0.15404 nm).

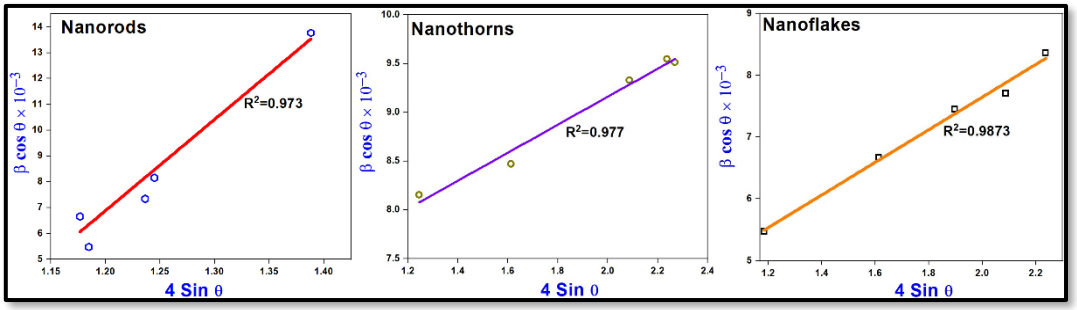

Fig. S4. Williamson−Hall (W−H) plots of ZnO nanostructures: nanorods, nanothorns, and nanoflakes.

The average strain values obtained from the W-H plots for the nanostructures, e.g., nanorod, nanothorn and nanoflake, are 3.5×10^{-3}, 1.4×10^{-3}, and $2.6\times10^{-3,}$ respectively. So, the nanorod is the most strained nanostructure, which is in line with the observed little peak shift in its XRD spectra of ZnO nanorods. The positive values of strain indicate the presence of the compressive nature of strain within the nanocrystal. The nanorods with the highest strain value have the smallest crystallite size, high degree of deformation and tilted growth over the ITO surface. The higher value of compressive strain in the nanoflake samples after nanorods indicates restraining growth along the c-axis, while growth along the other axis contributed to enhanced nanocrystallite size.

- **Rietveld Analysis**

The Rietveld refinement of the ZnO nanocrystals was carried out using Fullprof software to determine our samples' refined crystallographic parameters and match them. The roles of strain and crystal defect in broadening the peaks were neglected during refinement. The unit cell volume, occupancy site, lattice parameters, and atomic coordinates were refined using Rietveld refinement. The X-ray diffraction profile was fitted using the Pseudo-Voigt function. During refinement, the peak shape parameters and Caglioti parameters were refined. The background was refined using linear interpolation of the background points. After refining these parameters, systematic refinement of other parameters like occupancies, lattice parameters, FWHM and isotropic thermal parameters was done. The convergence of the Rietveld refinement achieved the best quality refinement to a satisfactory reliability value. The

modelling quality was scrutinized by the trustworthy values of R_{wp}, R_{exp}, Bragg *R*-factors and χ^2. The summary of the Rietveld analysis results for the nanoflakes and nanothorns is given in the Table S1.

Table S1. Values of lattice constants, the volume of the unit cell, $\chi^2$and R-factors obtained from Rietveld analysis

Sample Name	*a (Å)*	*b (Å)*	*c (Å)*	*V (Å³)*	*Goodness of Fit (χ^2)*	*R Factors*
1. Nanothorns	*3.2517 Å*	*3.2517 Å*	*5.209 Å*	*47.706 Å³*	*2.25*	*R_{wp}=8.80* *R_{exp}= 5.87* *R_{Braggs}= 1.09*
2. Nanoflakes	*3.2499 Å*	*3.2499 Å*	*5.2059 Å*	*47.617 Å³*	*2.93*	*R_{wp}=8.97* *R_{exp}= 5.242* *R_{Braggs}= 1.15*

S2. Absorption Spectra: calculation of bandgap and Urbach tail energies

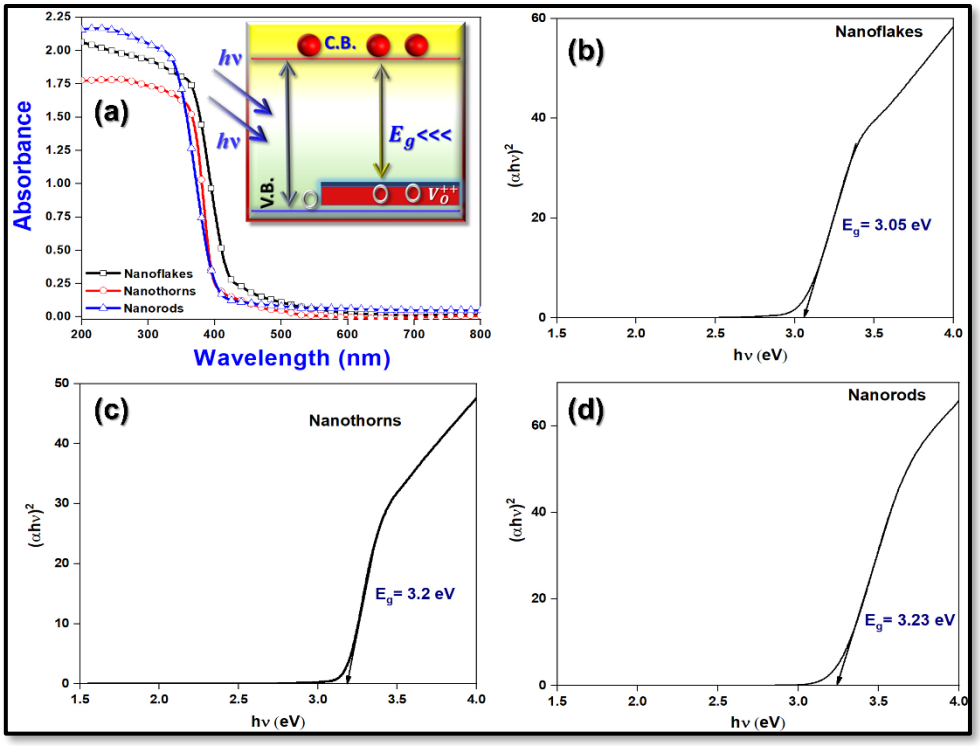

Fig. S5. (a) Absorption spectra of ZnO nanostructures with the inset schematic diagram demonstrate the bandgap narrowing induced by the presence of oxygen vacancy (V_O) on the surface of the nanoflake sample. Tauc plot of the (b) nanoflake. (c) nanothorn and (d) nanorod samples for determination of the band gaps.

From the absorption spectra of the nanostructures, as shown in Fig S5 (a), the band gap and the Urbach tail energies were calculated. The Urbach tail energy of the sample has been calculated using the formula (9):

$$\alpha(\upsilon) = \alpha_0 \exp\left(\frac{h\upsilon}{E_U}\right) \qquad (9)$$

Where, α_0 is a constant, E_U denotes energy which depends or remains constant with temperature change, and the tail width can be stated as the width of the localized states in the bandgap. The exponential tail is observed due to structural disorder in the crystalline material. The Urbach tail energy was determined from the slope of straight-line fitting in the plot of ln α vs *hν*. The band gap values obtained from Tauc plots, as shown in Fig S5 (b-d) for the nanorods, nanoflakes and nanothorns nanostructures, are 3.23

eV, 3.05 eV and 3.2 eV, respectively. In contrast, the corresponding Urbach tail energy values were obtained as 124 meV, 198 meV and 193 meV, respectively.

S3. Optical properties of different ZnO nanostructures

S3.1. PL emission properties of the TEOS-capped nanorods

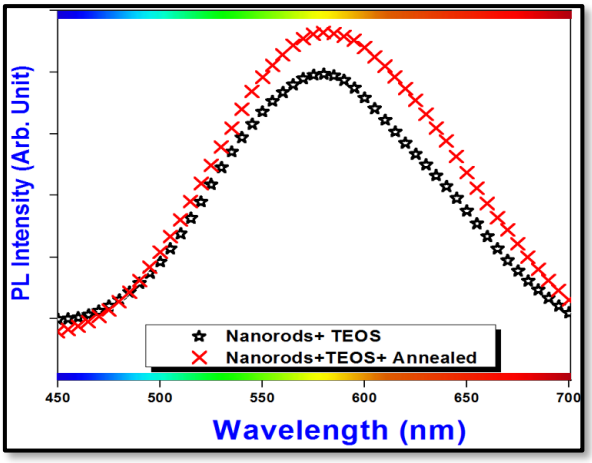

Fig. S6. Photoluminescence emission spectra of surface-modified ZnO nanorods at excitation wavelength 325 nm after surface modification (a) with TEOS and (b) after annealing the sample at 500℃.

S3.2. Details of the formation of different oxygen-related species on the ZnO nanostructures

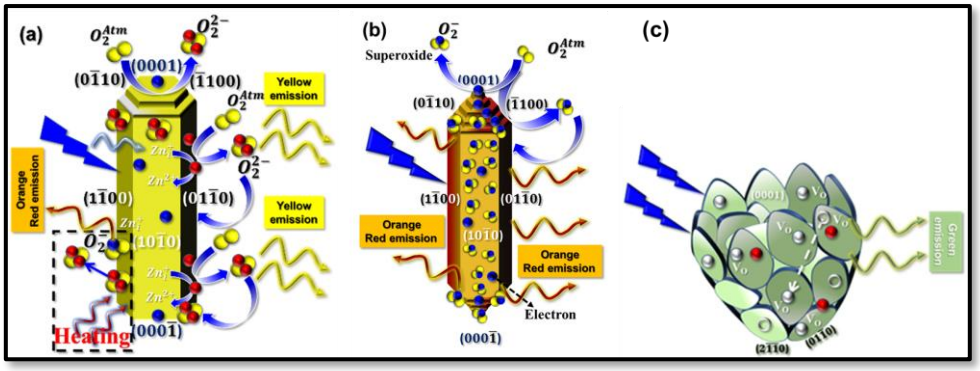

Fig. S7. (a) Generation and elimination of peroxide species on ZnO nanorods on (0001) planes. (b) superoxide species generation on nanoneedles surface (0001) polar and (10$\bar{1}$0) non-polar planes. (c) oxygen vacancy (V_O) based green emission from (0001) surface of nanoflakes.

- **XPS O(1s) core-level spectra of different nanostructures**

Table S2. XPS O (1s) core level spectra of different ZnO nanostructures

Samples	O_{Lat} (Area %)	V_O (Area %)	O_{Ads} (Area %)	V_O/O_{Lat}	O_{Ads}/ O_{Lat}
1. Nanorods	31.92 (529.9 eV)	14.6 (530.4 eV)	53.43 (531.4 eV)	0.46	1.67
2. Nanothorns	9.24 (530 eV)	18.16 (530.7 eV)	72.60 (531.6 eV)	1.97	7.86
3. Nanoflakes	52.98 (530.1 eV)	36.38 (531.3 eV)	10.63 (532.1 eV)	0.69	0.20

The detailed oxygen-related species adsorbed on the surface of the specific nanostructures (*nanorods, nanoneedles, and nanoflakes*) have been shown in Fig. S7 (a), (b), and (c), respectively. The quantitative and qualitative idea of the oxygen-related species can be found in the study of O(1s) spectra of the nanostructures, the results of which have been summarised in the table S2.

- **XPS Zn (2p) core-level spectra of as-synthesised and annealed nanorods**

The details of the peaks and the types of Zn present in the nanorods before and after annealing have been tabulated in table S3. This has been studied to investigate the presence of Zn_i's in the as-synthesised and annealed nanorods.

Table S3. The area under the peaks of the Zn (2p) XPS curve of the ZnO nanorod sample

Zn $2p_{3/2}$ (eV)	Zn $2p_{1/2}$ (eV)	Peak difference	Area %	Zn type	O_{Lat} /Zn
1. 1019.15	1. 1041.53	1. 22.38	1. 82.1	1. Lattice Zn	0.39
2. 1020.81	2. 1043.09	2. 22.28	2. 17.9	2. Mainly from Zn interstitial	
1. 1019.22 (Annealed)	1. 1042.09 (Annealed)	1. 22.87	×	1. Lattice Zn	×

Reasons behind Green emission from the nanoflakes: Grain boundaries in the polycrystalline nanostructure host a high density of oxygen vacancy (V_O) defect states, as seen in table S2. Grain boundaries are the sink for oxygen vacancies. In the case of polycrystalline structure, grain boundaries between adjacent crystals lead to the formation of a depletion layer[1]. These sites are responsible for oxygen adsorption rather than the surface. Physisorption of oxygen may occur in defect-free ZnO crystals. Still, if abundant oxygen vacancies are available in the grain boundaries, they play the primary centre for oxygen adsorption, which must have been the case in our nanoflake nanostructure. This chemisorbed oxygen causes band-bending-based green emission from the ZnO nanoflake nanostructure. The entire concept has been shown schematically in the Fig S10 (e).

Thus, the observed green emission in the nanoflakes results from the presence of oxygen vacancies below the crystallite surface, band-bending induced by oxygen adsorption at the grain boundaries, presence of sub-bandgap states, thermally activated trapping/de-trapping when excited below the band edge along with perturbation at the band edges due to band bending[2]. So, the simultaneous involvement of the three reasons mentioned above is responsible for the observed behaviour of green emissions from ZnO.

S4. De-convolution PL Spectra of different nanostructures

To get an idea of the contribution of different emission colours within the emission spectra, we de-convoluted the PL spectra using gaussian peaks, as shown in Fig. S8 and tabulated the results in table S4. Our findings [See Table S2 and S4] can easily explain all the contributions of emission colour from each nanostructure, as shown in Fig S8. In the case of the nanothorn sample, the green emission contribution is the least [See Table S4] among the nanostructures. This is because it contains an intermediate concentration of oxygen vacancy (V_O) coupled with the highest concentration of adsorbed oxygen species, which shadowed the effect of vacancy-based green emission, which may trap the electrons to generate the superoxide charge transfer state and reduces the chance of getting trapped in the defect states and participating in the green emission process from the nanothorn crystal. While in the case of nanorods with the least structural oxygen vacancy defect contribute to green emission due to oxygen adsorption-based band bending. Its band gap narrowing is also the least among all nanostructures, perfectly depicting the correlation with the least oxygen vacancy concentration. Also, green emission can be induced by below band gap excitation, while yellow and green emission can only

be induced by above band gap excitation. Our results match well with the results of Gasper et al.[3] , that yellow and green emission onset around 3 eV. Our observations contradict the observation by P.K. Giri et al.[4] and R. B. Lauer[5].

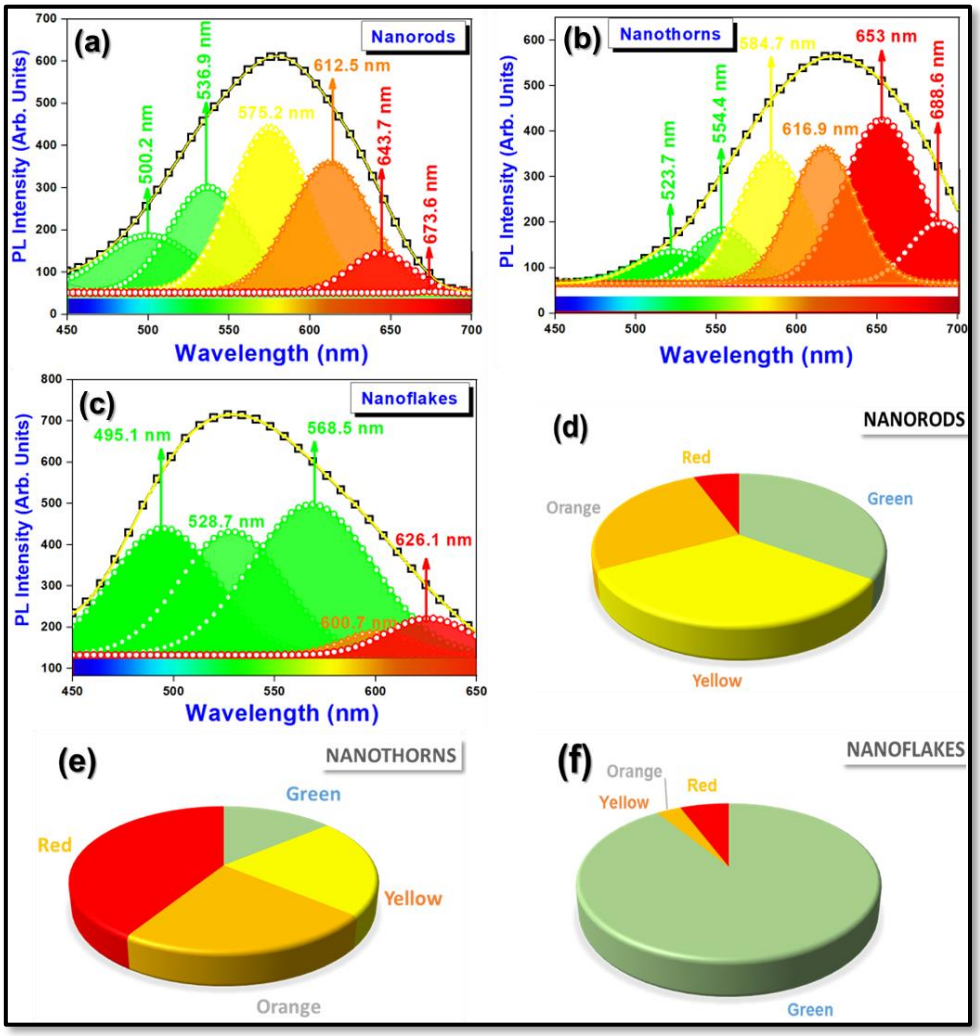

Fig. S8 De-convoluted photoluminescence spectra (excitation wavelength = 330 nm) of (a) Nanorod. (b) Nanothorn. (c) Nanoflake nanostructures. Pie chart showing the contribution of different visible emission colours in (d) Nanorod. (e) Nanothorn. (f) Nanoflake nanostructures.

Table S4. Percentage contribution of different emission colours from different ZnO nanostructures

Nanostructures	*Green*	*Yellow*	*Orange*	*Red*
1. Nanorods	*34*	*33*	*26*	*7*
2. Nanothorns	*14*	*22*	*23*	*41*
3. Nanoflakes	*91*	*0*	*2.7*	*6.3*

S5. Photocatalytic Activity of ZnO nanorods (as-prepared & annealed at 500 °C) and the corresponding mechanism: confirmation test for adsorbed oxygen species

The photocatalytic dye degradation of MO (given in the manuscript Fig 8) by the as-synthesised & annealed ZnO nanorod nanostructure has been discussed here. The Langmuir−Hinshelwood (L-H)

kinetic model is used to understand the degradation process. The (L−H) kinetic model has been employed to understand the photocatalytic dye degradation rate of methylene orange model dye by plotting the graph of ln (C/C_0) versus time, t, at different concentrations of dye. The relation for determining the photocatalytic dye degradation rate can be written as follows:

$$\ln\frac{C}{C_0} = -k_1 t \qquad (10)$$

The fitting of the plot using eq. (10) confirms that the nanorod follows pseudo-first-order degradation kinetics before and after annealing. The photocatalytic dye degradation efficiency percentage can be evaluated by using the relationship:

$$\text{Photocatalytic degradation efficiency \%} = \left(\frac{C_0 - C}{C_0}\right)\times 100\ \% \qquad (11)$$

- **The mechanism behind the observed PCA over nanorods**

The mechanism behind the PCA over nanorod nanostructure has been discussed here based on the radical scavenger test following the scheme proposed based on the experiments. At first, the photoexcited hole reacts with water to generate hydroxyl radical and hydrogen ions as per equation (12), while the peroxide species on the surface react with hydrogen ions to generate hydrogen peroxide according to equation (13). These generated hydrogen peroxide molecules get dissociated by the UV light to generate hydroxide radicals as per equation (14), or they capture photoexcited electrons to generate hydroxide ions or hydroxyl radicals as per equation (15). These reactive oxygen species (ROS) degrade the dye as per equation (16). The mechanism of photocatalytic dye degradation by the nanorods is given in Fig. S9.

$$h^+ + H_2O \longrightarrow H_2O^{\bullet+} \longrightarrow H^+ + OH^{\bullet} \qquad (12)$$

$$O_2^{2-} + 2H^+ \longrightarrow H_2O_2 \qquad (13)$$

$$H_2O_2 \xrightarrow{UV\ light} 2\,OH^{\bullet} \qquad (14)$$

$$H_2O_2 + e^- \longrightarrow OH^{\bullet} + OH^- \qquad (15)$$

$$OH^{\bullet} + Dye \longrightarrow Degraded\ by\text{-}product. \qquad (16)$$

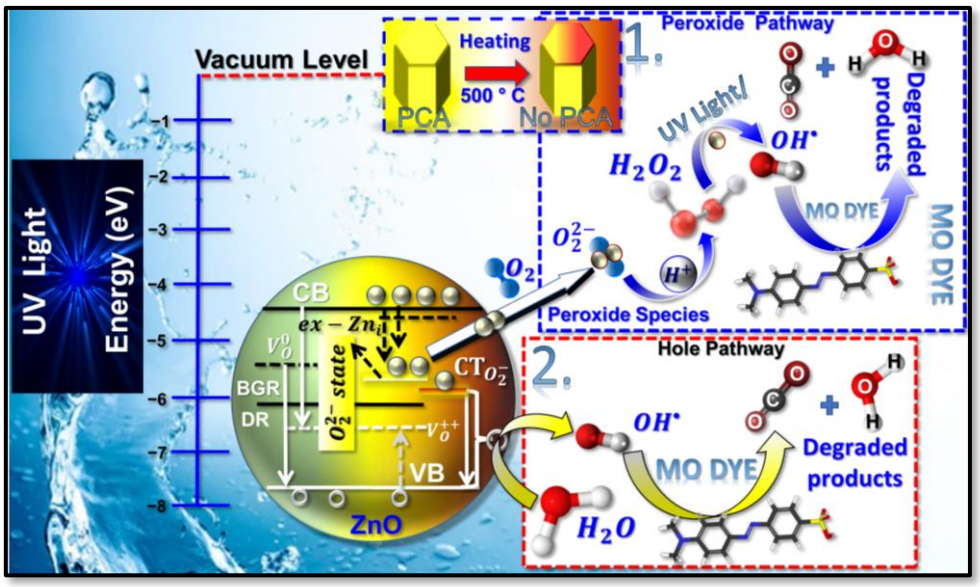

Fig. S9. Mechanism of photocatalytic dye-degradation depicting the presence of peroxide-type species promotes PCA in as synthesised nanorods, while the generation of superoxide charge transfer states

($CT_{O_2^-}$) in the annealed nanorods reduces the PCA by promoting radiative recombination of carriers in those states.

On annealing, the peroxide species over the surface is desorbed, and the reaction is hindered, significantly reducing the dye degradation ability. On annealing, the emission from the nanorod sample changes from yellow to orange-red. Consequently, the reduction in dye degradation efficiency confirms that the peroxide species are eliminated, and species corresponding to the proposed orange-red emission are formed, i.e., superoxide, which prefers radiative recombination over carrier separation. This confirms the presence of peroxide species (O_2^{2-}) over the as-synthesized ZnO nanorod samples and clarifies that superoxide (O_2^-) CT species replace the peroxide species on annealing. This demonstrates that superoxide formation over the nanostructure of ZnO must be prevented to design a promising photocatalyst using ZnO.

S6. Quantum yield and emission colour purity of the nanostructures

Quantum yield (QY) values of the ZnO samples have been calculated by the comparison method[6] with the quinine sulphate (r = reference dye) used as a reference dye using Eqn. (17). The known quantum yield of the reference dye is 0.546 in 0.5 M H_2SO_4. The excitation wavelength of the dye is 310 nm.

$$QY_{Samples} = QY_r \times \left(\frac{A_r}{A_s}\right) \times \left(\frac{E_s}{E_r}\right) \times \left(\frac{n_s}{n_r}\right)^2 \qquad (17)$$

A_s= Absorbance of the ZnO & surface modified ZnO samples in ethanol (< 0.1) was always kept under 0.1 to avoid the reabsorption effect, A_r= Absorbance of reference dye in 0.5 M H_2SO_4= 0.073, n_s = refractive index of ethanol = 1.36, n_r = refractive index of sulphuric acid = 1.346, E_s & E_r are integrated fluorescence intensity.

The purity of the emitted colour[7] can be calculated using the equation:

$$Colour\ purity = \frac{\sqrt{(x-x_i)^2+(y-y_i)^2}}{\sqrt{(x_d-x_i)^2+(y_d-y_i)^2}} \times 100\ \% \qquad (18)$$

Where (x, y) are the coordinates of samples, (x_i, y_i) are the coordinates of reference white light having the value (0.333, 0.333), and (x_d, y_d) are the coordinates of the dominant wavelength. The dominant light coordinates were chosen according to the NTSC organization as: (0.21,0.71) for green emission from the nanoflake sample, (0.67, 0.33) for red emission from the nanothorn sample and (0.438, 0.397) for yellow emission from nanorod sample. The colour coordinates of the samples have been determined using a chromaticity coordinate diagram, and the energy diagram showing the origin of different emissions has been given below.

Chromaticity coordinates & Energy diagram

The CIE plot of the nanorod, nanothorn, nanoflake, and annealed samples is shown in Fig. S10 (a), (b), (c) and (d). The energy band diagram showing the origin of different emissions from different nanostructures is shown in Fig. S10 (e). The schematic diagram of how different species evolved on the nanostructures of ZnO has been given in Fig. S7.

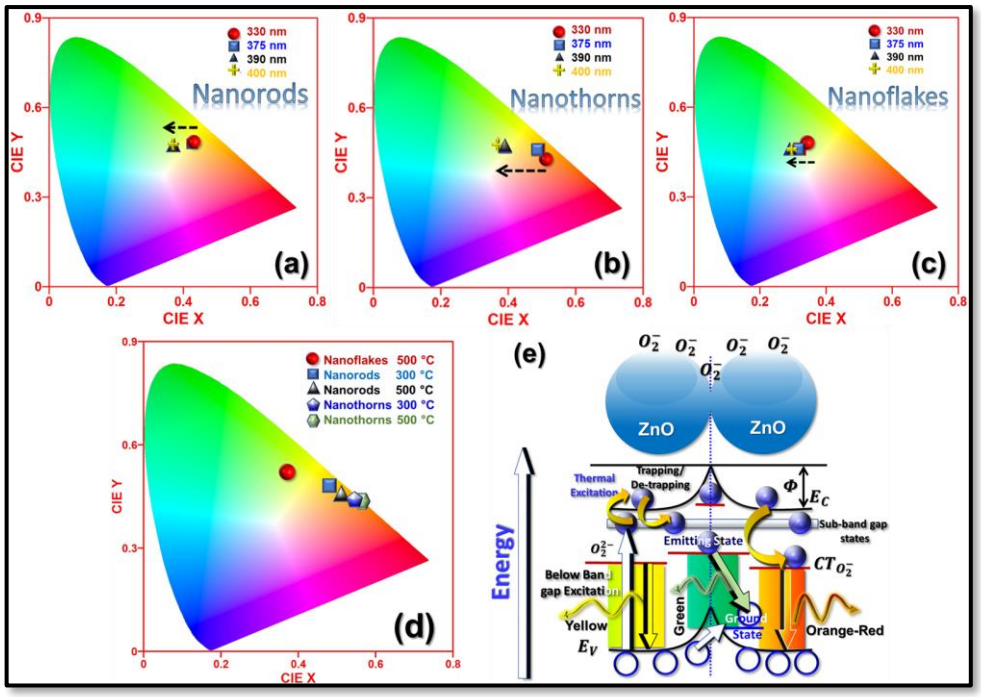

Fig. S10. CIE plots of (a) nanorods. (b) nanothorns. (c) nanoflakes. (d) nanorod, nanothorn and nanoflake samples were annealed at 300 °c and 500 °c. (e) Schematic diagram showing combined energy diagram to represent the role of different defects and adsorbed species behind visible emission from different nanostructures of ZnO.

S7. Tuneable LED application of different ZnO nanostructures

Here, we try to understand how different nanostructures of the same materials, i.e., ZnO, can be employed to design light-emitting diodes. The qualitative idea of the prototype LED that can be fabricated using these nanostructures can be obtained by calculating the device's internal/external quantum efficiency and power efficiency. Such LEDs can be tunable by changing the excitation energy or the concentration of different nanostructures while fabricating LED panels. Quantum efficiency is characterized by two types of efficiencies, namely internal and external quantum efficiency. The Quantum mechanics rule suggests that the ratio of singlet and triplet excitons that can form inside material will be generated in the ratio of 1:3. The ratio of the number of singlets to triplet excitons is $\frac{1}{4}:\frac{3}{4}$. The factor φ considers the fraction of carriers that participate in the exciton formation as the injected carriers can be lost by various other processes like charge injection barrier at anode or cathode etc. The internal quantum efficiency of the active material can be defined as the number of photons emitted by the material per injected carrier and can be mathematically expressed as:

$$\eta_{int}(\mathrm{EL}) = \frac{1}{4}\eta(PL)\ \varphi \qquad (19)$$

In the above equation, the values of $\eta(PL)$ for different nanostructures have been taken from the photoluminescence quantum yield of the different nanostructures. Another vital parameter for characterizing the property of a light-emitting diode is the external quantum efficiency which corresponds to the number of detectable photons per injected carrier and can be expressed mathematically as:

$$\eta_{ext}(\mathrm{EL}) = \frac{\eta_{int}(\mathrm{EL})}{2n^2} \qquad (20)$$

Where, *n* is the refractive index of the ZnO emissive layer in this calculation equal to 8.5. The external power efficiency factor takes the electrical properties of a fabricated light-emitting diode. The external

power efficiency is defined as the ratio of the power of the emitted light to the driving electrical power of the device. The factor can be expressed mathematically:

$$\eta_p \text{ (EL)} = \frac{\omega}{e\,V}\,\eta_{ext} \text{ (EL)} \qquad (21)$$

In the above equation, the ω is a variable based on the emission wavelength of the LED. Here, ω is the energy of the photon emitted by the LED of a particular wavelength, V is the working voltage of the LED, e is the elementary charge, and η_{ext}(EL) is the external quantum efficiency. The value of ω for green, yellow and orange-red emissions are 2.36 eV, 2.14 eV and 1.2 eV, respectively. The maximum possible power efficiency cannot be greater than the external quantum efficiency of the light-emitting material. So, when $\omega = eV$, the maximum power efficiency will be obtained. Therefore, it is not possible to obtain efficiency greater than η_{ext}(EL). So, corresponding to each energy value of the emitting light, the LED will work only in the range greater than the starting voltage and not on the voltage below it. So, in Fig. S11. (a), (b), and (c), we have a different working range of the LED with different starting voltages.

Based on the Langevin carrier recombination model for the injected carriers inside the prototype LED device, we can calculate the current density and number of singlet excitons generated inside it. The number of carriers that take part in the recombination, assuming the number of carriers injected per unit time per unit area to be equal to:

$$\frac{J}{e} = k_{e-h}N^2 d \qquad (22)$$

$$where, k_{e-h} = \frac{e\,(\mu_e+\mu_h)}{\varepsilon\varepsilon_0} \text{ is the recombination rate.}$$

In the equation, J is the current density, ε is the dielectric constant of ZnO = 8.5, e is the elementary charge, ε_0= 8.85×10^{-14} F cm^{-1} is the permittivity in a vacuum, d is the thickness of the emissive layer, μ_e *and* μ_h are the mobilities of electrons and holes inside the ZnO emissive layer after carrier injection. The mobility of the electron and holes is considered equal in the active emissive layer, equal to 1.7×10^{-4} cm^2 V^{-1} sec^{-1}.

Combining the above last two equations, we get the concentration of injected carriers to be equal to:

$$N = \frac{1}{e}\sqrt{\frac{J\varepsilon_0\varepsilon}{(\mu_e+\mu_h)d}} \qquad (23)$$

The number density of singlet excitons (n_s) that are generated inside the LED on injection of carriers can be written as:

$$n_s = \frac{1}{4}\frac{J\tau_S}{ed} \qquad (24)$$

The number of carriers injected into the device is twice those injected (considering holes and electrons together). The plots of the generation of singlet excitons corresponding to the injected carrier have also been shown in Fig. S11(d). This plot shows that the value of φ, the ratio of singlet excitons generated by the carrier's concentration, increases with current density.

From the results of the plot given in the Fig S11 (a-c), it can be seen that orange-red LED will have the highest efficiency when all the injected carriers participate (φ=1) in forming an exciton, followed by the yellow and green emitting LEDs, respectively. This goes well with the expectation and origin of each emission from the individual nanostructures. Green emitting nanoflakes have many oxygen vacancies and sub-bandgap states, so φ is expected to be low as well, which is the reason behind green emission, so it has the least external power efficiency among all the nanostructures. Next in the row is the yellow emission, which results from peroxide species generated due to Zn interstitial (Zn_i) defects, so it has low external power efficiency compared to orange-red emitting LED. Also, yellow-emitting LED has better external power efficiency than green emission because V_O is abundant compared to Zn_i and is present below the surface. Orange-red emitting LED has the highest external power efficiency because the emission is oxygen adsorption over the surface and takes place without the involvement of

the defect states. So, the result showed that oxygen species adsorption-based emission colour from ZnO nanoparticles could open up new avenues for high quantum yield colour-tuneable LEDs.

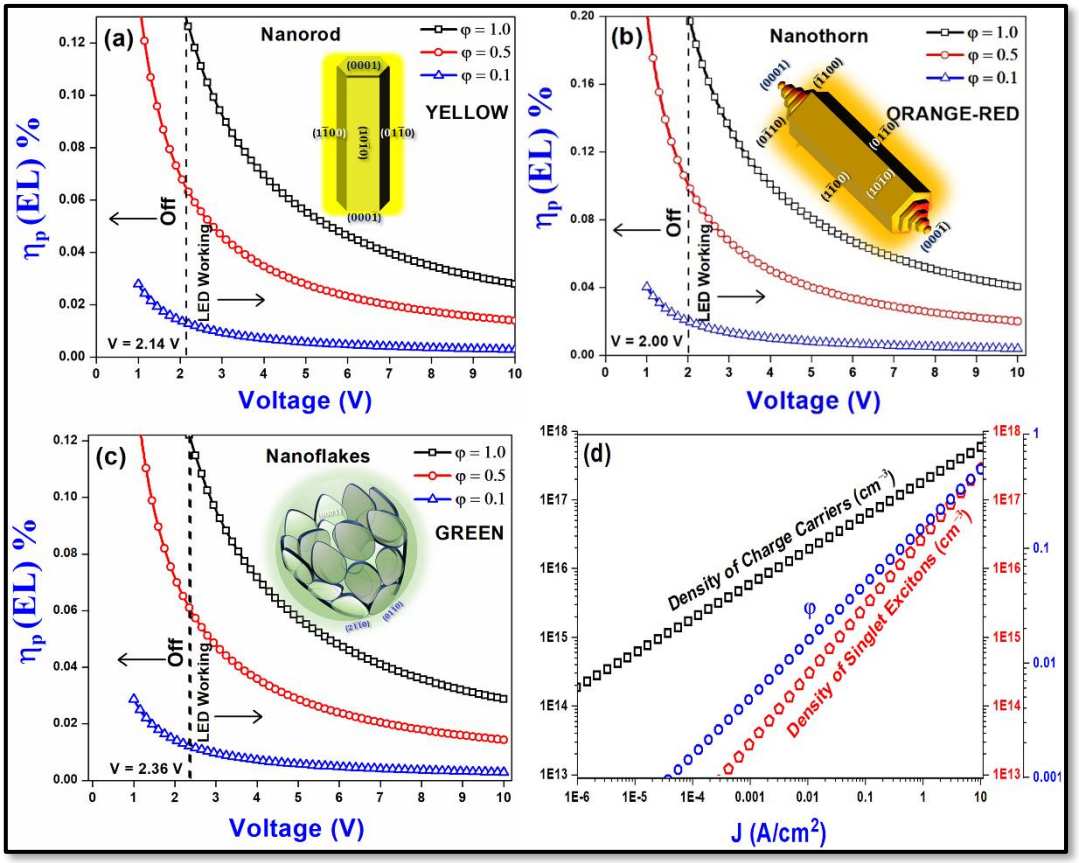

Fig. S11. Plot showing the variation of external power efficiency along with voltage for different dominant colour emitting nanostructures (a) Yellow by nanorods. (b) Orange-red by nanothorns. (c) green by nanoflakes. and (d) plots of the generation of singlet excitons and concentration of injected carriers inside the ZnO nanostructures based on Langevin's carrier recombination model.

S8. Photocatalytic dye degradation pathways for different nanostructures

- **A General dye degradation Scheme followed by ZnO nanostructures**

$ZnO + h\nu \longrightarrow e^- + h^+$

$h^+_{V_O} + V^0_O \longrightarrow V^+_O$ [Surface vacancy] [Also less available in nanothrons]

$V^+_O + h^+ \longrightarrow V^{++}_O$

$h^+ + H_2O \longrightarrow H_2O^{\bullet+} \longrightarrow H^+ + OH^\bullet$

$h^+ + OH^- \longrightarrow OH^\bullet$

[Hole trap at V_O]

$e^- + O_2 \longrightarrow O_2^-$

$e^-_{Zn_i} + O_2 \longrightarrow O_2^-$ [These species give rise to emissive states in the nanothorns]

[Electron trap at Zn_i]

$H_2O_2 \xrightarrow{UV\ light} 2\ OH^\bullet$

$OH^{\bullet}$ + dye ⟶ Degraded by product.

O_2^- + dye ⟶ Degraded by product.

Table S5. Results of photocatalytic dye degradation parameters displayed by different nanostructures

Samples	*Dye Degradation Efficiency (%)*	*Degradation rate constant (min^{-1})*
1. Nanoflakes	*81*	*0.01312*
2. Nanothorns	*27*	*0.00256*

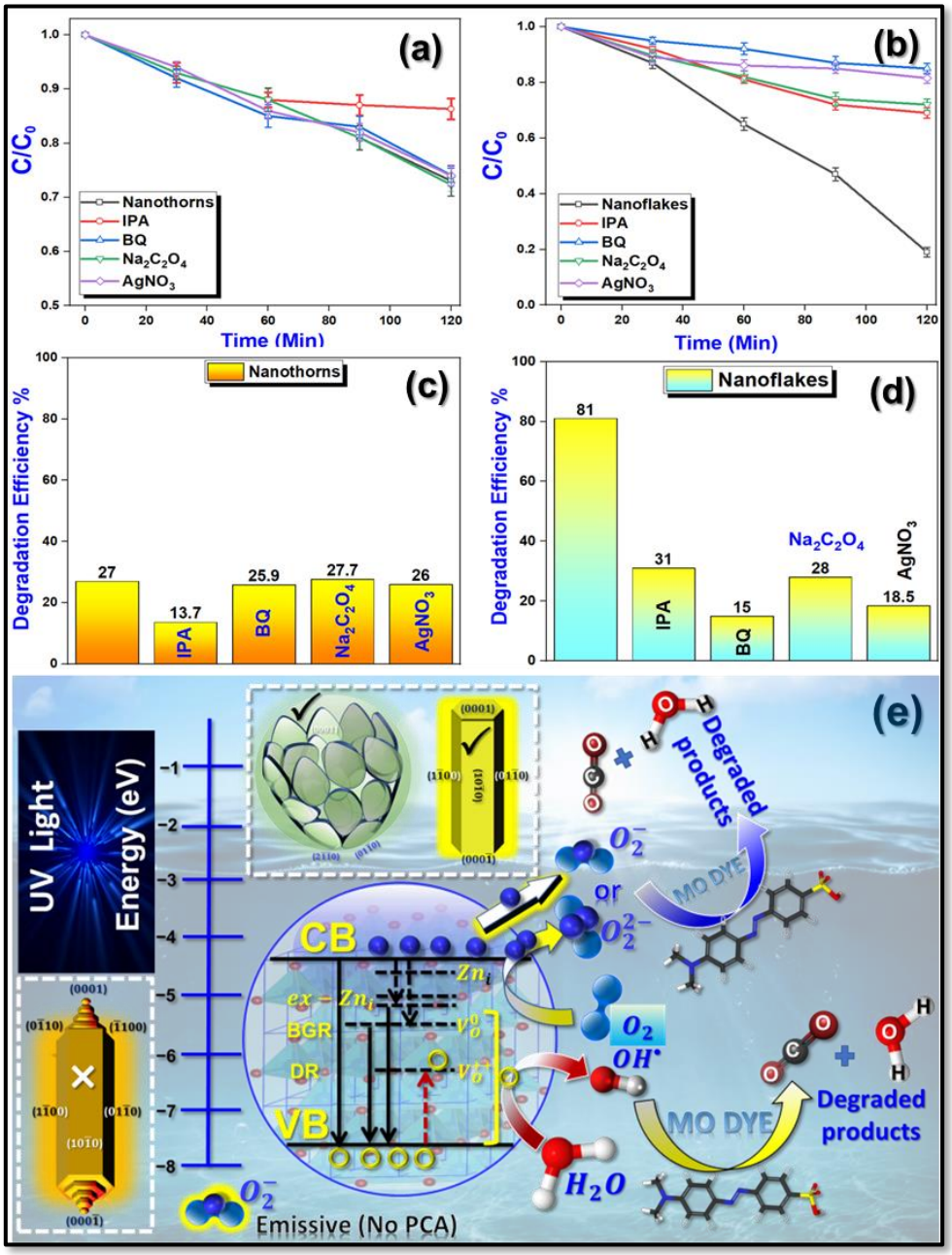

Fig.S12. (a) Photocatalytic degradation of the MO dye over nanothorns under irradiation of UV light in the presence and absence of radical scavengers. (b) Photocatalytic degradation of the MO dye over nanoflakes under irradiation of UV light in the presence and absence of radical scavengers. (c) Histogram showing evolution of dye degradation efficiency % of the nanothorns in the presence and absence of radical scavengers. (d) Histogram showing evolution of dye degradation efficiency % of the nanoflakes in the presence and absence of radical scavengers (e) Photocatalytic degradation mechanism depicting all the pathways contribution to efficient dye degradation: role of oxygen vacancy (V_O) and zinc interstitial (Zn_i) in case of the two nanostructures, e.g., nanoflakes and nanorods.

The experimental results of variation in the dye degradation ability of the nanostructures, e.g., nanothorns and nanoflakes in the presence of radical scavengers, have been given in Fig. S12 (a-d). The dye degradation mechanism followed by the nanostructures has been shown in Fig S12 (e).

S8.1. Reason behind photocatalytic activity difference in the nanostructures

Among the nanostructures, the nanoflakes have a large exposed (0001) plane with a high concentration of oxygen vacancy (V_O), which help to trap the photoexcited carriers and thus prohibits the recombination. This leads to the efficient generation of reactive oxygen species (ROS), which promote high PCA. In the case of nanorods with growth along [0001] direction, this leads to the diffusion of Zn_i^+ favourably which on interaction with molecular oxygen, gives rise to peroxide species. The formation of peroxide species on the surface of the nanorods gives rise to high PCA. While in the case of nanothorns with sharp structures in the [0001] direction enhances electron concentration, leading to the adsorption of more oxygen in superoxide by capturing those electrons. Also, the nanothorn has higher oxygen vacancy concentrations found at the grain boundaries, which further promotes oxygen chemisorption in the form of superoxide. Since the superoxide states are emissive, radiative recombination is preferred over the carrier separation necessary for high PCA. Due to this, the PCA of nanothorn is poor. The nanothorns also enjoy vectorial transport of photo-generated charge carriers among all nanostructures, so better adsorption of oxygen in the form of superoxide occurs. Oxygen adsorption also takes place on the non-polar plane $(10\bar{1}0)$. The reason behind the redshifting in emission on annealing is that on annealing, Zn_i turns optically inactive and also the non-polar surface $(10\bar{1}0)$ could adsorb oxygen giving rise to superoxide CT states. But, the gas adsorption ability of the surface ranges from (0001) > $\{10\bar{1}0\}$. So, nanothorns have weak PCA because it has emissive superoxide CT states where carriers prefer to recombine over carrier separation necessary for ROS generation and less exposed (0001) plane. Nanorods have high peroxide species content on the nanostructure surface facilitated by growth along the c-axis in the [0001] direction with the involvement of zinc interstitials. This peroxide species generates hydroxyl ions which degrade the dye as it is reactive oxygen species (ROS). So, the different exposed surfaces of morphologically different nanostructures have different species responsible for PCA in the ZnO nanostructures.

S8.2. Recyclability test on nanorod and nanoflake samples: Stability test

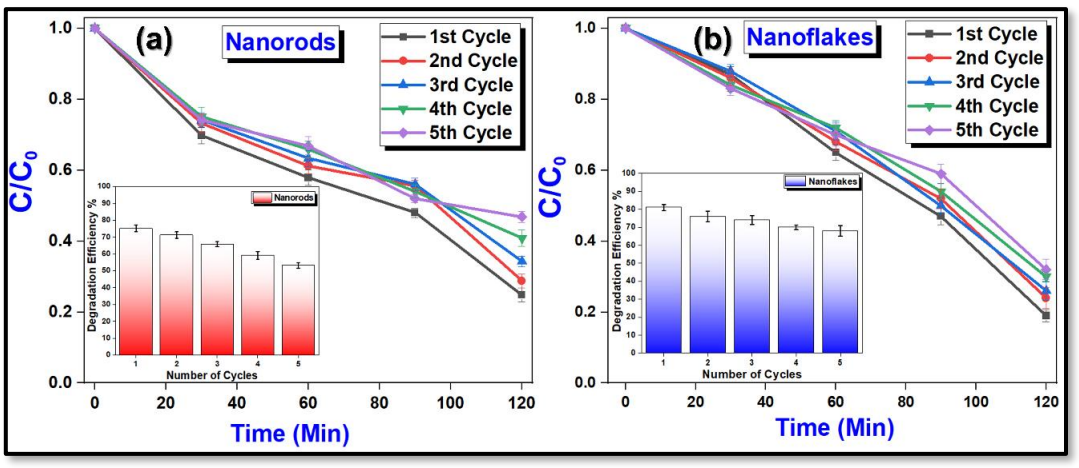

Figure S13. MO dye degradation by the (a) nanorods and (b) nanoflakes under five re-cycling episodes under UV light for 120 minutes, with the inset showing the evolution in the dye degradation efficiency with consecutive cycles.

References

[1] Peter M. Wojcik et al. *Nanotechnology*, 2021, **32**, 035202.
[2] Q. H. Li, T Gao, Y G Wang and T H Wang, *Appl. Phys. Lett.*, 2005, **86**, 123117.
[3] C. Gaspar, F. Costa, T. J. Monteiro, *Mater. Sci.: Mater. Electron.*, 2001, **12**, 269.
[4] R. K. Biroju, P. K. Giri, *J. Appl. Phys.*, 2017, **122**, 044302.
[5] R. B. Lauer, *J. Phys. Chem. Solids.*, 1973, **34**, 249.
[6] C. Würth, M. Grabolle, J. Pauli, M. Spieles, U. Resch-Genger. *Anal. Chem.* 2011, 83, **9**, 3431–3439.
[7] S. Das, C. Kr. Ghosh, R. Dey, M. Pal. *RSC Adv.*, 2016, **6**, 236-244.